International Journal of Advance Interdisciplinary Research
Vol. 2, Issue 3, Part A, (July-Sept) 2026, pp. 155-188, e-ISSN: 3107-913X
DOI: https://doi.org/10.66095/ijair.2026.v2.i3.a.9

Numerical Simulation and Optimization of a Lead-Free FTO/ZnO/$BaCoCl_3$/Cu_2O/Au Heterojunction Solar Cell Using SCAPS-1D

[1]K. C. Dubey, [2]Susheel Kumar Singh, [2*]R. K. Shukla, [3]Shobhit Shukla and [2]Anchal Srivastava
[1]Department of Physics, Shia P.G. College, Lucknow-226020
[2]Department of Physics, University of Lucknow, Lucknow-226007, INDIA
[3]Department of Information Technology, Dr. Shakuntala Misra National Rehabilitation University, Lucknow- 226017, INDIA
*Email: rajeshkumarshukla00@gmail.com,

Abstract

We report a comprehensive numerical investigation of a lead-free, inorganic heterojunction photovoltaic device based on the half-metallic ferromagnetic perovskite $BaCoCl_3$ as an absorber layer, sandwiched between a zinc oxide (ZnO) electron transport layer (ETL) and a cuprous oxide (Cu_2O) hole transport layer (HTL), with fluorine-doped tin oxide (FTO) as the front transparent electrode and gold (Au) as the back ohmic contact. All simulations were performed using Solar Cell Capacitance Simulator in one dimension (SCAPS-1D, version 3.3.10) under AM1.5G illumination (100 mW cm^{-2}) at 300 K. The baseline device (500 nm $BaCoCl_3$ absorber, intrinsic doping, defect density ~10^{16} cm^{-3}) yields an open-circuit voltage (V_{oc}) of 1.293 V, short-circuit current density (J_{sc}) of 12.07 mA cm^{-2}, fill factor (FF) of 85.14%, and power conversion efficiency (PCE) of 13.29%. Systematic optimization of absorber thickness (25–800 nm), donor doping (10^{10}–10^{22} cm^{-3}), and bulk trap density (10^{10}-10^{22} cm^{-3}) yields an optimized device with V_{oc} = 1.477 V, J_{sc} = 13.25 mA cm^{-2}, FF = 91.18%, and PCE = 17.84%, representing a 34.2% relative efficiency improvement over the baseline. The quantum efficiency (QE) spectrum confirms a sharp band-edge onset near 620 nm (~2.0 eV), consistent with the $BaCoCl_3$ bandgap. The effects of operating temperature (300–400 K), series resistance (R_s), shunt resistance (R_{sh}), and back-contact work function are systematically analyzed. The dominant loss mechanism in the baseline device is bulk Shockley–Read–Hall (SRH) recombination in the absorber, responsible for 7.67 mA cm^{-2} integrated recombination current. Shunt resistance below 10^3 Ω cm^2 catastrophically degrades performance (PCE < 4.4%). The Au back contact (work function 5.1 eV) is shown to provide near-ideal ohmic behaviour for Cu_2O. Our results demonstrate the photovoltaic potential of the novel FTO/ZnO/$BaCoCl_3$/Cu_2O/Au architecture as a viable inorganic, lead-free alternative to emerging perovskite solar cell technologies.

International Journal of Advance Interdisciplinary Research
Vol. 2, Issue 3, Part A, (July-Sept) 2026, pp. 155-188, e-ISSN: 3107-913X
DOI: https://doi.org/10.66095/ijair.2026.v2.i3.a.9

Keywords: $BaCoCl_3$, lead-free perovskite, ZnO electron transport layer, Cu_2O hole transport layer, SRH recombination, heterojunction solar cell, band alignment, defect engineering.

1. Introduction

The urgent transition from carbon-emitting energy sources to sustainable alternatives has elevated photovoltaics to the forefront of global energy research [1, 2]. Silicon solar cells have dominated the commercial market for decades, but their energy-intensive manufacturing, rigid form factors, and high material costs create barriers to widespread deployment [3]. The emergence of halide perovskite solar cells has transformed the efficiency landscape: within a single decade, perovskite power conversion efficiencies have surpassed 27%, a benchmark achieved by silicon only after decades of incremental improvement [4].

The conventional halide perovskites, particularly methylammonium lead iodide ($MAPbI_3$) and its compositional variants, owe their outstanding performance to near-optimal direct bandgaps (1.5–1.6 eV), extraordinarily high absorption coefficients (> 10^5 cm^{-1}), low exciton binding energies and long minority-carrier diffusion lengths exceeding 1 µm [5]. However, the intrinsic toxicity of lead (Pb^{2+}), its bioaccumulative nature, and strict regulatory scrutiny under the European RoHS Directive and analogous frameworks worldwide have fuelled an extensive search for lead-free photovoltaic absorbers [6, 7]. Candidate materials including tin (Sn), germanium (Ge), bismuth (Bi) and antimony (Sb) based perovskites have been extensively explored, yet each suffers from critical deficiencies: Sn^{2+} readily oxidizes to Sn^{4+}, introducing deep trap states; Ge-based perovskites exhibit poor ambient stability; Bi and Sb based compounds frequently adopt lower-dimensional crystal structures that impede efficient charge transport [8].

A fundamentally different class of lead-free absorbers, the barium cobalt trihalide perovskites $BaCoX_3$ (X = Cl, Br, I), has recently attracted attention owing to their half-metallic ferromagnetic character, theoretically predicted by density functional theory (DFT) calculations [9, 10]. $BaCoX_3$ compounds adopt the cubic perovskite (*Pm*3*m*) crystal structure and exhibit: (i) spin-polarized electronic structures with one spin channel showing metallic behaviour and the other semiconducting; (ii) tunable bandgaps across the visible spectrum (E_g ≈ 2.1, 1.6 and 1.2 eV for Cl, Br and I, respectively); (iii) elevated carrier mobility's (40–50

International Journal of Advance Interdisciplinary Research
Vol. 2, Issue 3, Part A, (July-Sept) 2026, pp. 155-188, e-ISSN: 3107-913X
DOI: https://doi.org/10.66095/ijair.2026.v2.i3.a.9

$cm^2\ V^{-1}\ s^{-1}$) attributed to low effective masses in the ferro-magnetically ordered state; and (iv) negligible ionic radii mismatch ensuring crystallographic stability [11, 12]. The chloride compound, $BaCoCl_3$, presents the largest bandgap in the family (~2.1 eV), positioning it as a potential wide-bandgap absorber suitable for tandem configurations or standalone devices demanding high V_{oc}.

Critically, the choice of charge transport layers profoundly governs the photovoltaic performance of any heterojunction device. Zinc oxide (ZnO) is an attractive ETL candidate owing to its large bandgap (3.2 - 3.4 eV), high electron mobility (~200 $cm^2\ V^{-1}\ s^{-1}$), solution processability, and well - matched conduction band alignment with many halide perovskites [13]. Cuprous oxide (Cu_2O) is a naturally abundant, non-toxic, earth - abundant p-type semiconductor with bandgap ~2.17 eV and long hole diffusion length (>1 µm in high-quality single crystals), making it an ideal inorganic HTL that eliminates the thermal instability and hygroscopicity problems associated with organic hole transporters such as Spiro-OMeTAD [14, 15].

Despite the promise of the $BaCoX_3$ family, no experimental solar cell device using these absorbers has been reported to date and existing simulation studies have focused exclusively on the TiO_2/Spiro-OMeTAD transport layer combination [9]. The FTO/ZnO/$BaCoCl_3$/Cu_2O/Au architecture-employing fully inorganic, earth-abundant charge transport layers-remains entirely unexplored in the literature. This work presents, to the best of our knowledge, the first numerical simulation study of the FTO/ZnO/$BaCoCl_3$/Cu_2O/Au heterojunction, conducted using the industry-standard SCAPS-1D simulator.

The objectives of this study are to: (1) establish baseline photovoltaic performance; (2) characterize the J-V curve, quantum efficiency, energy-band diagram, and carrier transport profiles; (3) systematically analyze the effects of absorber thickness, doping, and defect density; (4) evaluate the sensitivity to temperature, series and shunt resistance, and back-contact work function; (5) identify the dominant loss mechanisms; and (6) define the optimized device configuration and benchmark it against reported lead-free and comparable solar cell architectures.

2. Device Architecture and Physical Background

2.1 Layer Structure and Function

The proposed device is structured as:

International Journal of Advance Interdisciplinary Research
Vol. 2, Issue 3, Part A, (July-Sept) 2026, pp. 155-188, e-ISSN: 3107-913X
DOI: https://doi.org/10.66095/ijair.2026.v2.i3.a.9

FTO/ZnO/$BaCoCl_3$/Cu_2O/Au (back contact → HTL → absorber layer → ETL → front transparent electrode, with illumination incident from the FTO side) as shown in Fig. 1.

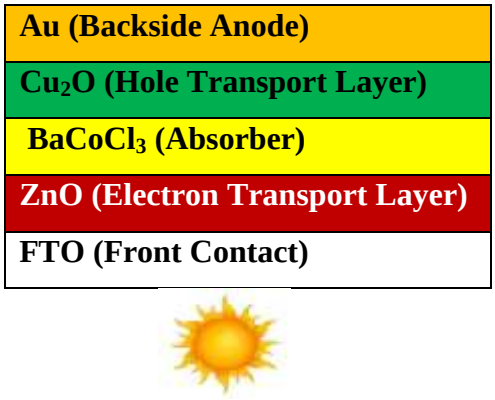

Fig. 1: Plan structure of FTO/ZnO/$BaCoCl_3$/Cu_2O/Au - based solar cell.

In the SCAPS-1D simulation framework, the device extends from x = 0 (Au back contact) to x = L (FTO front electrode through which AM1.5G illumination enters). Table 1 summarizes the layer thicknesses and doping concentrations used in the baseline and optimized simulations.

Table 1: Material and device parameters used in the SCAPS-1D simulations of the FTO/ZnO/$BaCoCl_3$/Cu_2O/Au device.

Parameter	FTO	ZnO (ETL)	$BaCoCl_3$ (Absorber)	Cu_2O (HTL)
Thickness (nm)	100	100	500 (baseline) / 800 (optimized)	100
Bandgap E_g (eV)	3.50	3.30	2.02	2.17
Electron affinity χ (eV)	4.00	3.75	3.95	3.0
Doping type	n	n	intrinsic (base.) / n (opt.)	p
Doping density (cm^{-3})	$N_D = 2\times10^{19}$	$N_D = 10^{21}$	10^{16} (base.) / 10^{22} (opt.)	$N_A = 10^{19}$
Carrier mobility μ_n/μ_p($cm^2/V\cdot s$)	20/10	200/25	50/40	20/80
Relative permittivity ε_r	9.00	9.0	4.6	7.5

International Journal of Advance Interdisciplinary Research
Vol. 2, Issue 3, Part A, (July-Sept) 2026, pp. 155-188, e-ISSN: 3107-913X
DOI: https://doi.org/10.66095/ijair.2026.v2.i3.a.9

Parameter	FTO	ZnO (ETL)	$BaCoCl_3$ (Absorber)	Cu_2O (HTL)
Bulk trap density (cm^{-3})	10^{15}	10^{15}	10^{15} (base.) / 10^{13} (opt.)	10^{15}
Back contact				Au, φ = 5.1 eV

Simulation parameters for $BaCoCl_3$ derived from DFT calculations [9–11]. ZnO and Cu_2O parameters from established literature [13–15].

Each layer performs a distinct function:

- **FTO (fluorine-doped SnO_2):** Highly transparent ($E_g \approx 3.5$ eV), heavily n-doped TCO ($N_D = 2 \times 10^{19}$ cm^{-3}) that allows solar photons to pass through while providing ohmic contact to the ZnO ETL. Its wide bandgap (3.5 eV) renders it transparent to above-gap photons.
- **ZnO (electron transport layer):** With $E_g \approx 3.3$ eV and $N_D = 10^{21}$ cm^{-3}, ZnO provides a selective pathway for photo-generated electrons while forming an energy barrier to holes. The conduction band minimum of ZnO forms a favourable offset with $BaCoCl_3$, enabling efficient electron extraction with minimal voltage loss.
- **$BaCoCl_3$ (absorber):** The central photovoltaic active layer with $E_g \approx 2.02$ eV (as determined from the QE onset in the simulation). Its absorption of photons with energy > E_g generates electron–hole pairs, which separate under the built-in electric field established at the heterojunctions.
- **Cu_2O (hole transport layer):** With $E_g \approx 2.17$ eV and $N_A = 10^{19}$ cm^{-3} (p-type), Cu_2O selectively extracts holes from the absorber valence band while blocking electrons. Cu_2O is notable for its high hole mobility (~100 cm^2 V^{-1} s^{-1} in crystalline form) and deep valence band, ensuring excellent hole selectivity.
- **Au (back contact):** A high-work-function metal (φ = 5.1 eV) that forms a near-ohmic contact with the p-type Cu_2O surface, enabling efficient hole collection without significant contact resistance.

2.2 Band Alignment and Carrier Selectivity

The photovoltaic principle relies on spatially separated selective contacts: electrons must be extracted toward FTO and holes toward Au. Effective carrier separation requires careful

International Journal of Advance Interdisciplinary Research
Vol. 2, Issue 3, Part A, (July-Sept) 2026, pp. 155-188, e-ISSN: 3107-913X
DOI: https://doi.org/10.66095/ijair.2026.v2.i3.a.9

control of conduction-band offsets (CBO) and valence-band offsets (VBO) at the $ZnO/BaCoCl_3$ and $BaCoCl_3/Cu_2O$ interfaces as given by Eq. (1) and (2).

For $ZnO/BaCoCl_3$:

$$\Delta E_C = \chi_{ZnO} - \chi_{BaCoCl3} \quad (1)$$

$$\Delta E_C = \chi_{ZnO} - \chi_{BaCoCl3} \quad (2)$$

A small spike or slightly negative CBO (cliff) at the ETL/absorber interface is generally preferred: a large positive spike (> 0.3 eV) creates an electron extraction barrier, while a moderate negative cliff (0 to −0.3 eV) facilitates electron flow without generating interface recombination as given by Eq. (3). The simulation band diagrams confirm type-II staggered alignment at this interface.

For $BaCoCl_3/Cu_2O$:

$$\Delta E_V = E_{V,BaCoCl3} - E_{V,Cu2O} \quad (3)$$

The valence band of Cu_2O must lie below (or align with) that of $BaCoCl_3$ to drive hole transfer from the absorber to the HTL. A favorable positive VBO (cliff) at this interface facilitates hole extraction.

From the SCAPS-1D band diagram data:

- **ZnO midpoint** (optimized): E_c = 1.319 eV, E_v = −1.981 eV, E_g = 3.300 eV
- **$BaCoCl_3$ midpoint** (optimized): E_c = 1.262 eV, E_v = −0.755 eV, E_g = 2.017 eV
- **Cu_2O midpoint** (optimized): E_c = 2.214 eV, E_v = 0.044 eV, E_g = 2.170 eV

The conduction band offset at $ZnO/BaCoCl_3$ is approximately −0.057 eV (small cliff), which facilitates electron extraction. The valence band offset at $BaCoCl_3/Cu_2O$ indicates alignment that supports hole extraction into Cu_2O.

3. Materials and Methods

3.1 Simulation Framework

All numerical simulations were conducted using **SCAPS-1D (Solar Cell Capacitance Simulator, version 3.3.10)**, developed and maintained by the Department of Electronics and Information Systems at Ghent University, Belgium [16]. SCAPS-1D numerically solves the coupled Poisson equation and the continuity equations for electrons and holes in one spatial dimension as given by Eqs. (4-6):

$$\frac{\partial^2 \psi}{\partial x^2} = -\frac{q}{\varepsilon}(p - n + N_D^+ - N_A^- + \rho_{defect}) \quad (4)$$

$$\frac{\partial n}{\partial t} = \frac{1}{q}\frac{\partial n}{\partial x} + G - R \quad (5)$$

International Journal of Advance Interdisciplinary Research
Vol. 2, Issue 3, Part A, (July-Sept) 2026, pp. 155-188, e-ISSN: 3107-913X
DOI: https://doi.org/10.66095/ijair.2026.v2.i3.a.9

$$\frac{\partial p}{\partial t} = -\frac{1}{q}\frac{\partial p}{\partial x} + G - R \quad (6)$$

where ψ is the electrostatic potential, q is the elementary charge, ε is the local permittivity, n and p are the free electron and hole concentrations, N_D^+ and N_A^- are the ionized donor and acceptor concentrations, G is the optical generation rate, and R is the net recombination rate. Carrier transport is treated by the drift–diffusion model given by Eq. (7-8):

$$J_n = q\mu_n nE + qD_n\frac{\partial n}{\partial x} \quad (7)$$

$$J_p = q\mu_p pE + qD_p\frac{\partial p}{\partial x} \quad (8)$$

where E is the electric field, $\mu_{n,p}$ are the carrier mobility's, and $D_{n,p} = \mu_{n,p}kBT/q$ are the diffusion coefficients (Einstein relation).

SCAPS-1D is a one-dimensional device simulator and therefore assumes perfect crystal uniformity in the lateral directions. Interface effects are approximated by planar defect distributions. Optical generation is computed using the transfer matrix method applied to the AM1.5G spectral irradiance profile, assuming the standard spectrum file AM1.5G 1 sun.spe with an incident power of 100 mW cm^{-2}.

3.2 Material Parameters

The simulation parameters are compiled in **Table 1**. $BaCoCl_3$ material properties were derived from peer-reviewed DFT calculations, as no experimental device data exist for this material [9–11]. ZnO and Cu_2O parameters were drawn from established literature and validated simulation databases [13–15].

$BaCoCl_3$ parameters:

- Bandgap (E_g): 2.1 eV (DFT-predicted; simulation-confirmed optical onset ~2.02 eV)
- Electron affinity (χ): estimated from DFT band structure calculations
- Carrier mobility (μ_n/μ_p): 50/40 $cm^2\ V^{-1}\ s^{-1}$ (half-metallic, low effective mass)
- Absorption coefficient: > 10^4 cm^{-1} (direct-gap absorber)
- Baseline defect density (N_t): ~10^{15} cm^{-3} (baseline device)

ZnO ETL parameters:

- E_g = 3.30 eV (simulation); electron affinity $\chi \approx$ 4.13.75 eV
- Relative permittivity $\varepsilon_r \approx 9.0$
- Electron mobility ≈ 100 $cm^2\ V^{-1}\ s^{-1}$
- Donor concentration $N_D = 10^{21}$ cm^{-3}

International Journal of Advance Interdisciplinary Research
Vol. 2, Issue 3, Part A, (July-Sept) 2026, pp. 155-188, e-ISSN: 3107-913X
DOI: https://doi.org/10.66095/ijair.2026.v2.i3.a.9

- Thickness: 100 nm

Cu_2O HTL parameters:

- E_g = 2.17 eV; HOMO level ≈ 5.4 eV
- Acceptor concentration $N_A = 10^{19}$ cm^{-3}
- Hole mobility ≈ 80 cm^2 V^{-1} s^{-1}
- Thickness: 100 nm

3.3 Simulation Conditions

All simulations used the following boundary conditions:

- Illumination: AM1.5G, 100 mW cm^{-2}, neutral density filter $N_D = 0$
- Temperature: 300 K
- Voltage range: 0 to 1.3 V (baseline) / 1.48 V (optimized) in 0.02 V steps
- Frequency: 10^6 Hz (for AC simulations)
- Front contact: FTO (ohmic, selective electron contact)
- Back contact: Au, work function φ = 5.1 eV

3.4 Defect and Interface Modeling

Bulk SRH recombination is computed using the standard two-level trapping model as given by Eq. (9):

$$R_{SRH} = \frac{np - n_i^2}{\tau_p(n+n_1)+\tau_n(p+p_1)} \quad (9)$$

Where $n_1 = n_i \exp(\frac{E_t - E_i}{kT})$ and $p_1 = n_i \exp(\frac{E_i - E_t}{kT})$, with E_t the trap energy level and E_i the intrinsic Fermi level. The carrier lifetimes $\tau_n = \frac{1}{v_{th}\sigma_n N_t}$ and $\tau_p = \frac{1}{v_{th}\sigma_p N_t}$ depend on the thermal velocity v_{th}, capture cross sections $\sigma_{n,p}$ and trap density N_t.

Interface recombination is incorporated as a thermionic emission/recombination current at the ETL/absorber and absorber/HTL interfaces. In the baseline device, mid-gap traps (E_t at the intrinsic level) with capture cross sections $\sigma_n = \sigma_p = 10^{-15}$ cm^2 were assumed.

4. Results and Discussion

4.1 Baseline Photovoltaic Performance

Table 2 summarizes the baseline device performance extracted from the SCAPS-1D J-V simulation. The baseline configuration consists of: FTO/ZnO (100 nm, $N_D = 10^{21}$ cm^{-3})/$BaCoCl_3$ (500 nm, intrinsic)/Cu_2O (100 nm, $N_A = 10^{19}$ cm^{-3})/Au.

Table 2: Baseline photovoltaic performance of the FTO/ZnO/$BaCoCl_3$ (500 nm)/Cu_2O/Au device under AM1.5G, 100 mW cm^{-2}, 300 K.

International Journal of Advance Interdisciplinary Research
Vol. 2, Issue 3, Part A, (July-Sept) 2026, pp. 155-188, e-ISSN: 3107-913X
DOI: https://doi.org/10.66095/ijair.2026.v2.i3.a.9

Parameter	Value	Unit
Open-circuit voltage (V_{oc})	1.293	V
Short-circuit current density (J_{sc})	12.069	mA cm^{-2}
Fill factor (FF)	85.14	%
Power conversion efficiency (PCE, η)	13.29	%
Maximum power point voltage (V_{MPP})	1.142	V
Maximum power point current (J_{MPP})	11.633	mA cm^{-2}

A V_{oc} of 1.293 V is notably high for a single-junction solar cell under AM1.5G illumination. This is a direct consequence of the wide bandgap of $BaCoCl_3$ (~2.1 eV). Using the theoretical relationship for V_{oc} as given by Eq. (10):

$$V_{OC} = \frac{nk_BT}{q}\ln(\frac{J_{sc}}{J_0} + 1) \quad (10)$$

a high J_{sc}/J_0 ratio implies reduced dark recombination, consistent with the moderate defect density in $BaCoCl_3$ for the baseline case. The PCE of 13.29% is limited by a J_{sc} of only 12.07 mA cm^{-2} - a consequence of the relatively wide bandgap restricting absorption to wavelengths below ~620 nm-and by non-negligible SRH recombination at the baseline defect density.

The relationship between PCE, V_{oc}, J_{sc}, and FF is given by Eq. (11):

$$PCE\ (\eta) = V_{oc} \cdot J_{sc} \cdot FF \cdot P_{in} \times 100\% \quad (11)$$

where P_{in}=100 mW cm^{-2}. For the baseline device:

η = 1.293×12.069×0.8514×100 = 13.29%

Confirming numerical consistency of the SCAPS-1D output.

4.2 J–V Characteristics and Quantum Efficiency

The full J-V curve as shown in Fig. 2 confirms a highly rectified, near-ideal diode response:

- The curve is flat (nearly constant J_{sc}) from 0 to ~1.10 V, indicating low series resistance and effective carrier collection in this regime.
- The current onset (roll-over) begins near V = 1.15 V, with the knee becoming increasingly evident toward V_{oc}.
- At V = 1.20 V: J = −10.35 mA cm^{-2}, indicating the onset of increased recombination current.
- At V = 1.28 V: J = −2.45 mA cm^{-2}; at V = 1.30 V: J = +1.43 mA cm^{-2} (crosses zero).

International Journal of Advance Interdisciplinary Research
Vol. 2, Issue 3, Part A, (July-Sept) 2026, pp. 155-188, e-ISSN: 3107-913X
DOI: https://doi.org/10.66095/ijair.2026.v2.i3.a.9

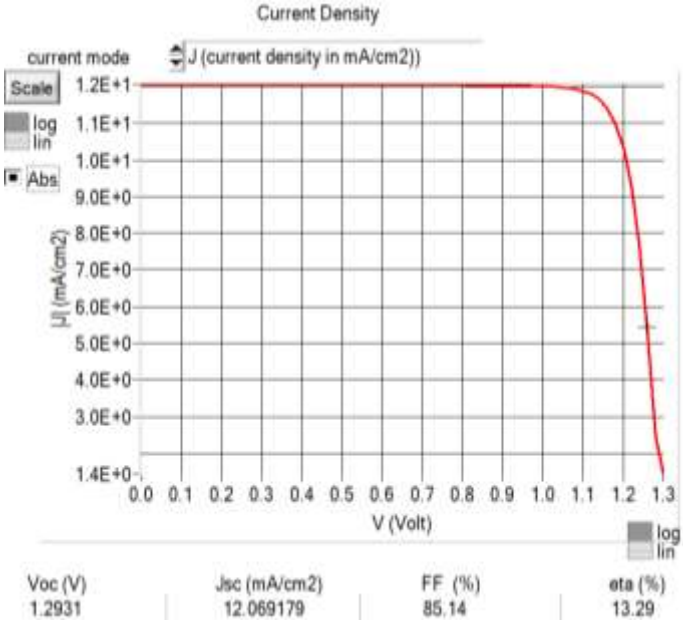

Fig. 2: J–V characteristic curve of the baseline FTO/ZnO/BaCoCl3/Cu2O/Au device under AM1.5G illumination (100 mW cm-2, 300 K). Key photovoltaic parameters: Voc = 1.293 V, Jsc = 12.07 mA cm-2, FF = 85.14%, PCE = 13.29%.

Recombination current analysis from the J–V table reveals that bulk SRH recombination (J_{SRH}) dominates throughout the voltage range: at V = 0, J_{SRH} = 0.00157 mA cm^{-2}, rising to 7.665 mA cm^{-2} at V = 1.30 V. Interface recombination is smaller (3.76×10^{-5} mA cm^{-2} at V = 0), growing to 5.83 mA cm^{-2} near open-circuit. Radiative and Auger recombination are absent (zero) under these conditions, confirming that SRH is the exclusive recombination channel in the SCAPS-1D model for this system.

Quantum efficiency (QE) spectrum:

The simulated QE rises from 75.6% at 300 nm to a peak of ~99.1% at 360 nm, remains above 90% from 360 – 490 nm, and then declines progressively as shown in Fig. 3:

- 500 nm: 92.4%
- 550 nm: 83.6%
- 580 nm: 70.6%
- 600 nm: 54.4%
- 610 nm: 35.7%
- ≥ 620 nm: < 10% (essentially zero)

The sharp QE cut-off at 620 nm corresponds to a photon energy of 2.00 eV, consistent with the $BaCoCl_3$ bandgap of ~2.1 eV (the 20 nm redshift relative to the bandgap is characteristic of Urbach tail absorption). The QE at short wavelengths (< 360 nm) is reduced due to

International Journal of Advance Interdisciplinary Research
Vol. 2, Issue 3, Part A, (July-Sept) 2026, pp. 155-188, e-ISSN: 3107-913X
DOI: https://doi.org/10.66095/ijair.2026.v2.i3.a.9

parasitic absorption in the FTO and ZnO front layers before photons reach the absorber. The high peak QE (99%) indicates excellent internal quantum efficiency with minimal interface recombination losses in the absorber at short wavelengths.

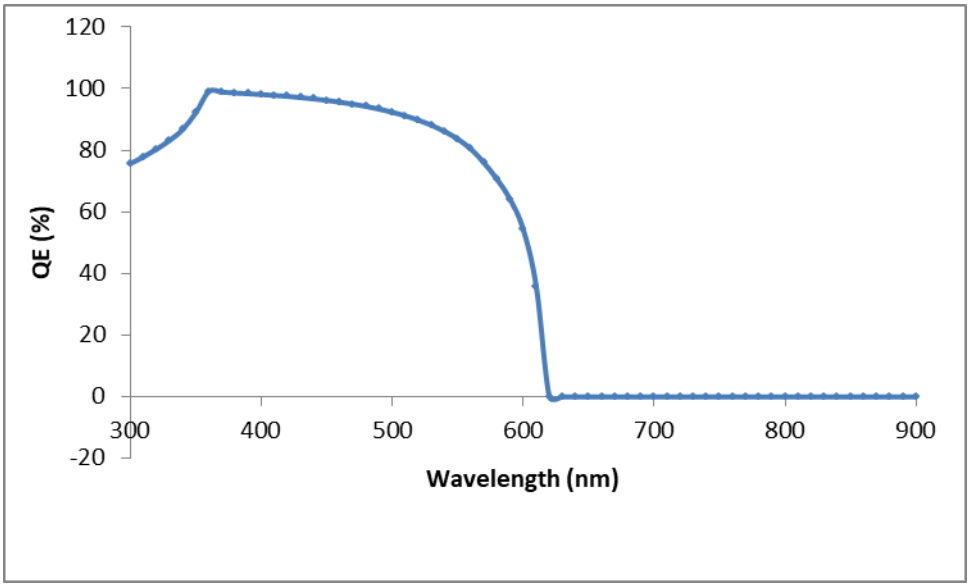

Fig. 3: QE plots for base performing device structure.

The short-circuit current calculated from the QE is given by Eq.(12):

$$J_{SC} = q \int_{\lambda_{min}}^{\lambda_{max}} QE(\lambda)\phi_{AM1.5G}(\lambda)d\lambda \qquad (12)$$

is consistent with the directly simulated J_{sc} = 12.07 mA cm^{-2}, validating the optical and electrical models.

4.3 Effect of Absorber Thickness

Table 3 presents the effect of $BaCoCl_3$ absorber thickness on device photovoltaic parameters, swept from 25 to 800 nm.

Table 3: Variation of absorber thickness on device photovoltaic parameters.

Thickness (nm)	V_{oc} (V)	J_{sc} (mA cm^{-2})	FF (%)	PCE (%)
25	1.2783	3.322	88.24	3.75
50	1.2886	4.380	88.76	5.01
100	1.3012	6.159	88.71	7.11
200	**1.3087**	8.674	88.39	10.03
300	1.3051	10.281	87.68	11.76
500	1.2931	12.069	85.14	13.29
600	1.2879	12.580	83.84	13.58

International Journal of Advance Interdisciplinary Research
Vol. 2, Issue 3, Part A, (July-Sept) 2026, pp. 155-188, e-ISSN: 3107-913X
DOI: https://doi.org/10.66095/ijair.2026.v2.i3.a.9

Thickness (nm)	V_{oc} (V)	J_{sc} (mA cm^{-2})	FF (%)	PCE (%)
700	1.2833	12.951	82.64	13.73
750	1.2812	13.098	82.02	13.76
800	1.2792	13.227	81.46	**13.78**

Physical interpretation:

J_{sc} increases monotonically with absorber thickness, rising from 3.32 mA cm^{-2} at 25 nm to13.23 mA cm^{-2} at 800 nm-a nearly 4× improvement. Thicker absorbers generate more photocurrent by capturing photons with longer absorption depths, particularly in the 450-620 nm range where the Beer-Lambert generation profile extends deep into the film. However, the rate of J_{sc} improvement diminishes beyond 500 nm as the absorber approaches optical saturation as shown in Fig. 4.

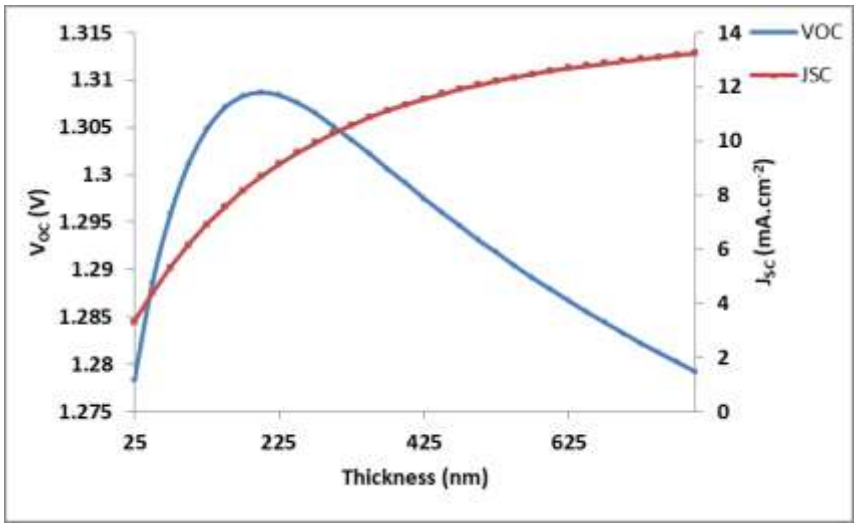

International Journal of Advance Interdisciplinary Research
Vol. 2, Issue 3, Part A, (July-Sept) 2026, pp. 155-188, e-ISSN: 3107-913X
DOI: https://doi.org/10.66095/ijair.2026.v2.i3.a.9

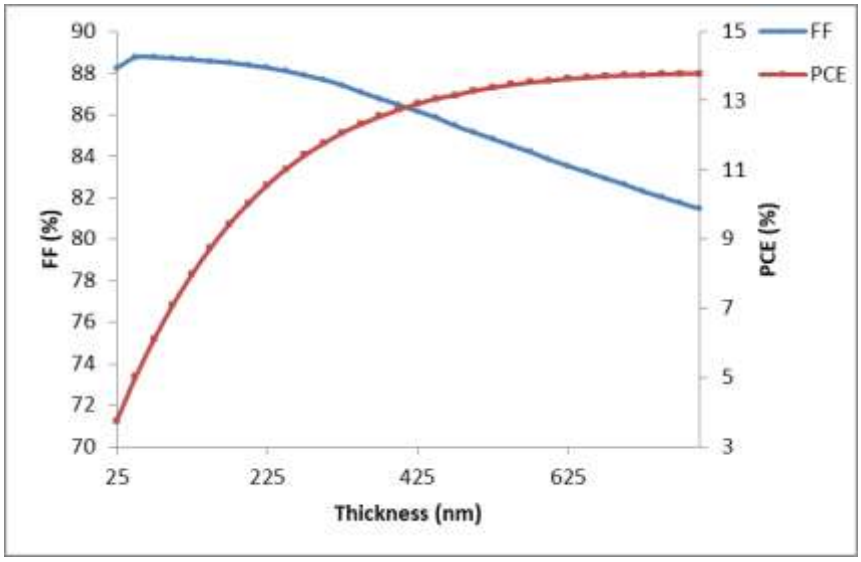

Fig. 4: Variation of the thickness of $BaCoCl_3$ (Absorber layer) on simulated parameters of solar cell.

V_{oc} shows a non-monotonic response: it rises from 1.278 V at 25 nm to a peak of **1.309 V at 200 nm**, then decreases steadily to 1.279 V at 800 nm. The initial V_{oc} increase reflects increasing photogenerated carrier density as J_{sc} rises. The subsequent decline is characteristic of increasing SRH recombination in the additional absorber volume: for a device limited by bulk recombination, $V_{oc} \propto -(E_g/(2q)) + (kBT/q) \times \ln(J_{sc}/J_0)$, and as $J_0 \propto N_t \times d$ (trap density × thickness), V_{oc} decreases with thickness.

FF decreases monotonically from 88.24% at 25 nm to 81.46% at 800 nm. This trend reflects the increasing recombination losses: in the thick absorber, carriers generated far from the junction must diffuse over longer distances, increasing the probability of trap capture and consequently reducing the shunting of carriers by recombination before extraction.

PCE increases from 3.75% to 13.78% as thickness grows from 25 to 800 nm. There is no clear optimum within the studied range under baseline (high trap density) conditions-PCE is still rising at 800 nm. This contrasts with typical thin-film absorbers where a PCE maximum is observed at the carrier diffusion length; the absence of a clear maximum suggests that the diffusion length in the baseline device (with ~10^{16} cm^{-3} trap density) may exceed 800 nm, or that the simulation did not extend to sufficient thickness to observe the rollover.

4.4 Effect of Absorber Doping (Donor Concentration N_D)

Table 4 summarizes the effect of $BaCoCl_3$ donor doping concentration (N_D) on photovoltaic performance.

International Journal of Advance Interdisciplinary Research
Vol. 2, Issue 3, Part A, (July-Sept) 2026, pp. 155-188, e-ISSN: 3107-913X
DOI: https://doi.org/10.66095/ijair.2026.v2.i3.a.9

Table 4: Variation of $BaCoCl_3$ donor doping concentration (ND) on photovoltaic performance

N_D (cm^{-3})	V_{oc} (V)	J_{sc} (mA cm^{-2})	FF (%)	PCE (%)
10^{10}	1.3088	13.057	85.70	14.65
10^{11}	1.3088	13.057	85.70	14.65
10^{12}	1.3088	13.057	85.70	14.65
10^{13}	1.3088	13.057	85.70	14.65
10^{14}	1.3087	13.058	85.69	14.64
10^{15}	1.3075	13.070	85.58	14.63
10^{16}	1.2792	13.227	81.46	13.78
10^{17}	1.3285	12.971	87.76	15.12
10^{18}	1.3307	12.915	87.42	15.02
10^{19}	1.3281	12.898	84.27	14.44
10^{20}	1.3585	12.895	88.42	15.49
10^{21}	1.4165	12.894	90.35	16.50
10^{22}	**1.4764**	12.892	**91.16**	**17.35**

Physical interpretation: The performance is virtually constant for N_D from 10^{10} to 10^{13} cm^{-3} (PCE ≈ 14.65%), confirming that at low doping levels, the device behaviour is intrinsic-like and governed by minority-carrier recombination dynamics rather than the background doping.

An anomalous dip occurs at $N_D = 10^{16}$ cm^{-3} (PCE = 13.78%), where V_{oc} drops to 1.279 V and FF degrades to 81.46%. This coincides with the region where the donor doping begins to compete with the intrinsic carrier concentration and potentially distorts the electric field distribution at the ZnO/$BaCoCl_3$ interface as shown in Fig. 5.

International Journal of Advance Interdisciplinary Research
Vol. 2, Issue 3, Part A, (July-Sept) 2026, pp. 155-188, e-ISSN: 3107-913X
DOI: https://doi.org/10.66095/ijair.2026.v2.i3.a.9

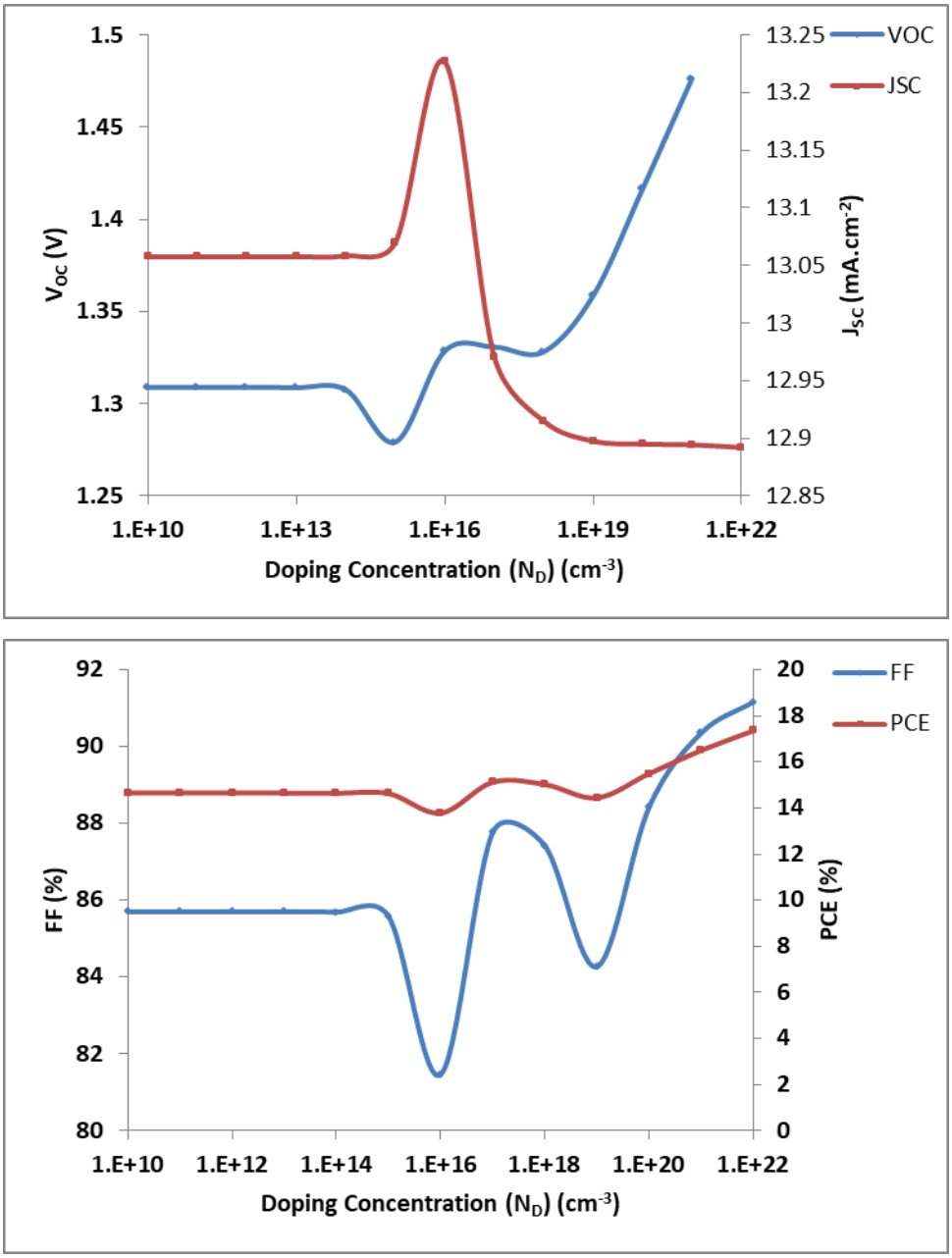

Fig. 5: Variation of doping concentration (N_D) of $BaCoCl_3$ on the simulated parameters of solar cell.

For $N_D > 10^{17}$ cm^{-3}, V_{oc} increases systematically with doping (1.328 → 1.476 V), while J_{sc} decreases slightly (13.23 → 12.89 mA cm^{-2}). The V_{oc} improvement with increased n-type doping is attributable to the enhanced built-in potential (V_{bi}) at the $BaCoCl_3/Cu_2O$ junction is given by Eq.(13):

$$V_{bi} = \frac{k_B T}{q} \ln\left(\frac{N_A N_D}{n_i^2}\right) \qquad (13)$$

International Journal of Advance Interdisciplinary Research
Vol. 2, Issue 3, Part A, (July-Sept) 2026, pp. 155-188, e-ISSN: 3107-913X
DOI: https://doi.org/10.66095/ijair.2026.v2.i3.a.9

With N_D increasing from 10^{16} to 10^{22} cm^{-3} and $N_A = 10^{19}$ cm^{-3} in Cu_2O, the built-in potential increases by approximately 6 × (60 mV) = 360 mV (6 decades of doping × 60 mV/decade), consistent with the observed V_{oc} increase from 1.279 to 1.476 V (+197 mV, slightly less due to Fermi-level pinning effects).

FF improves markedly from 81.46% at $N_D = 10^{16}$ to 91.16% at $N_D = 10^{22}$ cm^{-3}, because higher doping concentrates the depletion region into the absorber near the Cu_2O interface, shortening the distance over which minority holes must diffuse and reducing the relative impact of recombination on the series resistance of the device.

The slight J_{sc} decrease at high N_D reflects the onset of free-carrier absorption in the heavily doped absorber and a narrowing of the photo-generating volume as the depletion region shifts.

Key finding: Heavy donor doping at $N_D = 10^{22}$ cm^{-3} delivers a PCE of 17.35%-a 18.4% relative improvement over the PCE of 14.65% at low doping-driven primarily by a 13% increase in V_{oc} and a 6.4% increase in FF.

4.5 Effect of Absorber Defect (Trap) Density

Table 5 presents the effect of $BaCoCl_3$ bulk trap density (N_t) on device performance.

Table 5: Variation of device performance by the variation of trap density in $BaCoCl_3$.

N_t (cm^{-3})	V_{oc} (V)	J_{sc} (mA cm^{-2})	FF (%)	PCE (%)
10^{10}	1.4772	13.249	91.18	**17.84**
10^{11}	1.4772	13.249	91.18	17.84
10^{12}	1.4772	13.249	91.18	17.84
10^{13}	1.4772	13.245	91.17	17.84
10^{14}	1.4771	13.212	91.17	17.79
10^{15}	1.4764	12.892	91.16	17.35
10^{16}	1.4702	10.339	90.92	13.82
10^{17}	1.4388	3.167	90.26	4.11
10^{18}	1.3834	0.004	88.45	0.49
10^{19}	1.3489	0.001	85.42	0.13
10^{20}	1.3289	0.005	83.57	0.06
10^{21}	1.3220	0.004	84.37	0.05

International Journal of Advance Interdisciplinary Research
Vol. 2, Issue 3, Part A, (July-Sept) 2026, pp. 155-188, e-ISSN: 3107-913X
DOI: https://doi.org/10.66095/ijair.2026.v2.i3.a.9

Physical interpretation:

The defect density sweep reveals three distinct regimes:

Regime I ($N_t \leq 10^{13}$ cm^{-3}): Defect-tolerant high-performance zone. Performance is essentially invariant: PCE = 17.84%, V_{oc} = 1.477 V, J_{sc} = 13.25 mA cm^{-2}, FF = 91.18%. In this regime, the minority-carrier lifetime $\tau = (v_{th}\ \sigma\ N_t)^{-1}$ >> transit time, meaning virtually all photo-generated carriers are collected before recombination. The $BaCoCl_3$ absorber exhibits impressive defect tolerance in this doping-optimized configuration.

Regime II ($10^{14} \leq N_t \leq 10^{16}$ cm^{-3}): Transition zone. J_{sc} begins to degrade significantly: from 13.21 mA cm^{-2} at $N_t = 10^{14}$ to 10.34 mA cm^{-2} at $N_t = 10^{16}$ (a 21.7% reduction). V_{oc} declines from 1.477 to 1.470 V. PCE drops from 17.79% to 13.82% as shown in Fig. 6.

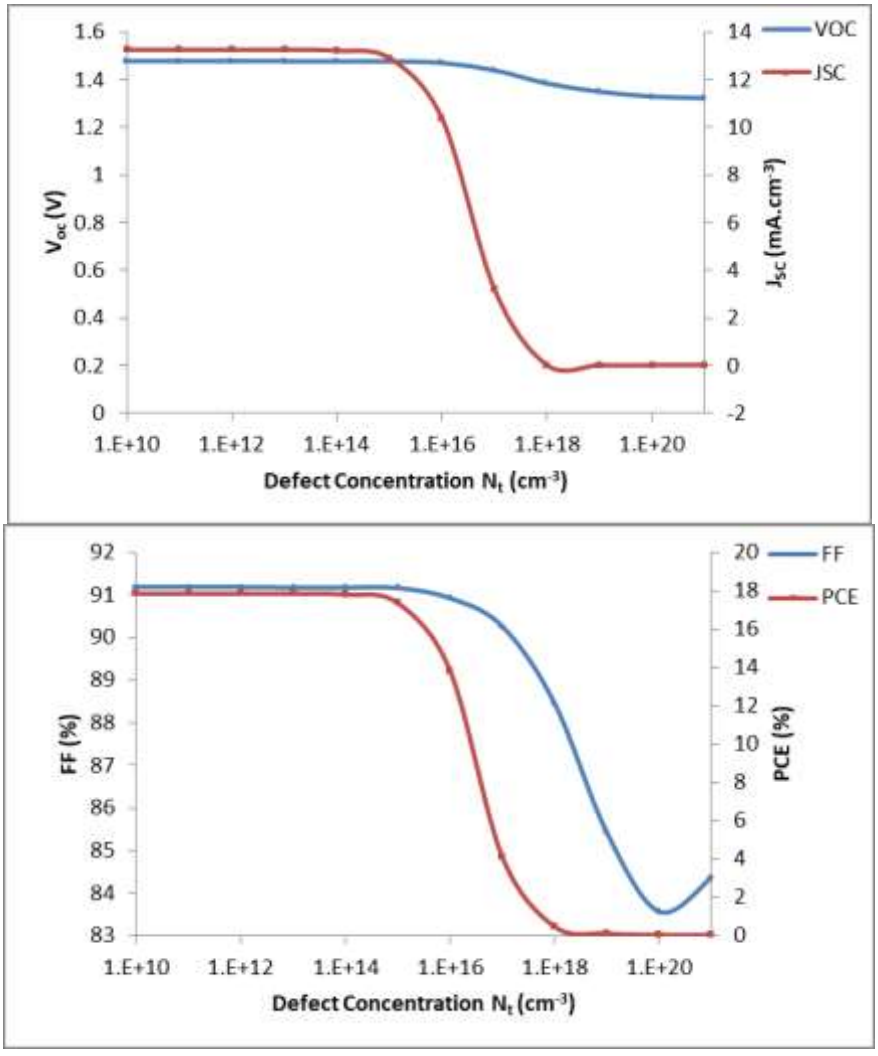

Fig. 6: Variation of the defect density of Absorber layer $BaCoCl_3$ on simulated parameters of solar cell.

The onset of SRH recombination is governed by Eq. (14):

International Journal of Advance Interdisciplinary Research
Vol. 2, Issue 3, Part A, (July-Sept) 2026, pp. 155-188, e-ISSN: 3107-913X
DOI: https://doi.org/10.66095/ijair.2026.v2.i3.a.9

$$\tau_{min} = \frac{1}{N_t \sigma v_{th}} \quad (14)$$

With $\sigma = 10^{-15}$ cm^2, $v_{th} \approx 10^7$ cm s^{-1}, the transition from negligible to significant SRH recombination occurs around $N_t = 10^{15}$–10^{16} cm^{-3}, consistent with the observed sharp degradation.

Regime III ($N_t \geq 10^{17}$ cm^{-3}): Device collapse. PCE drops catastrophically to 4.11% at $N_t = 10^{17}$ cm^{-3} and essentially zero (0.05–0.49%) for $N_t \geq 10^{18}$ cm^{-3}. J_{sc} collapses to < 0.005 mA cm^{-2} at $N_t \geq 10^{18}$ cm^{-3}, indicating that diffusion lengths have fallen below the absorber thickness. The minority-carrier diffusion length $L = D\tau^{1/2}$ scales as $N_t^{-1/2}$; at $N_t = 10^{18}$ cm^{-3}, L is estimated at < 50 nm, far below the 800 nm absorber thickness. V_{oc}, though reduced to 1.32-1.38 V, remains finite because the quasi-Fermi level splitting persists even with catastrophically poor carrier collection.

Critical finding: The defect-tolerant regime extends to $N_t \leq 10^{13}$ cm^{-3}, and practical device performance (PCE > 10%) requires $N_t < 10^{16}$ cm^{-3}. This places $BaCoCl_3$ in a favorable category: with a bulk trap density of 10^{15} cm^{-3} (achievable in solution-processed thin films), a PCE of 17.35% is predicted.

4.6 Effect of Series and Shunt Resistance

Variation of device performance by the Series resistance is shown in Table 6 (R_s = 0–10 Ω cm^2):

Table 6: Variation of device performance by the Variation of series resistance.

Rs (Ω cm^2)	V_{oc} (V)	J_{sc} (mA cm^{-2})	FF (%)	PCE (%)
0	1.4772	13.249	91.18	17.84
2	1.4775	13.249	89.42	17.51
5	1.4778	13.249	86.81	17.00
9	1.4780	13.249	83.35	16.32
10	1.4780	13.249	52.49	16.15

Series resistance reduces FF by creating an ohmic voltage drop, described by:

$$J = J_{SC} - J_0[\exp\left(\frac{q(V+JR_S)}{nk_BT}\right) - 1] \quad (15)$$

FF decreases from 91.18% at $R_s = 0$ to 83.35% at $R_s = 9$ Ω cm^2 (a nearly linear decrease of ~0.88% per Ω cm^2). A dramatic FF collapse to 52.49% occurs at $R_s = 10$ Ω cm^2, suggesting

International Journal of Advance Interdisciplinary Research
Vol. 2, Issue 3, Part A, (July-Sept) 2026, pp. 155-188, e-ISSN: 3107-913X
DOI: https://doi.org/10.66095/ijair.2026.v2.i3.a.9

non-linear resistance coupling at high values. Critically, V_{oc} is nearly unaffected by R_s (changing by only 0.8 mV over the studied range), confirming that V_{oc} is governed by recombination at open-circuit (where J = 0 and R_s plays no role). The PCE decreases by 9.5% relative (17.84% → 16.15%) over the 0–10 Ω cm^2 range. For practical devices, R_s < 3 Ω cm^2 is required to maintain PCE > 17.5% as shown in Fig. 7.

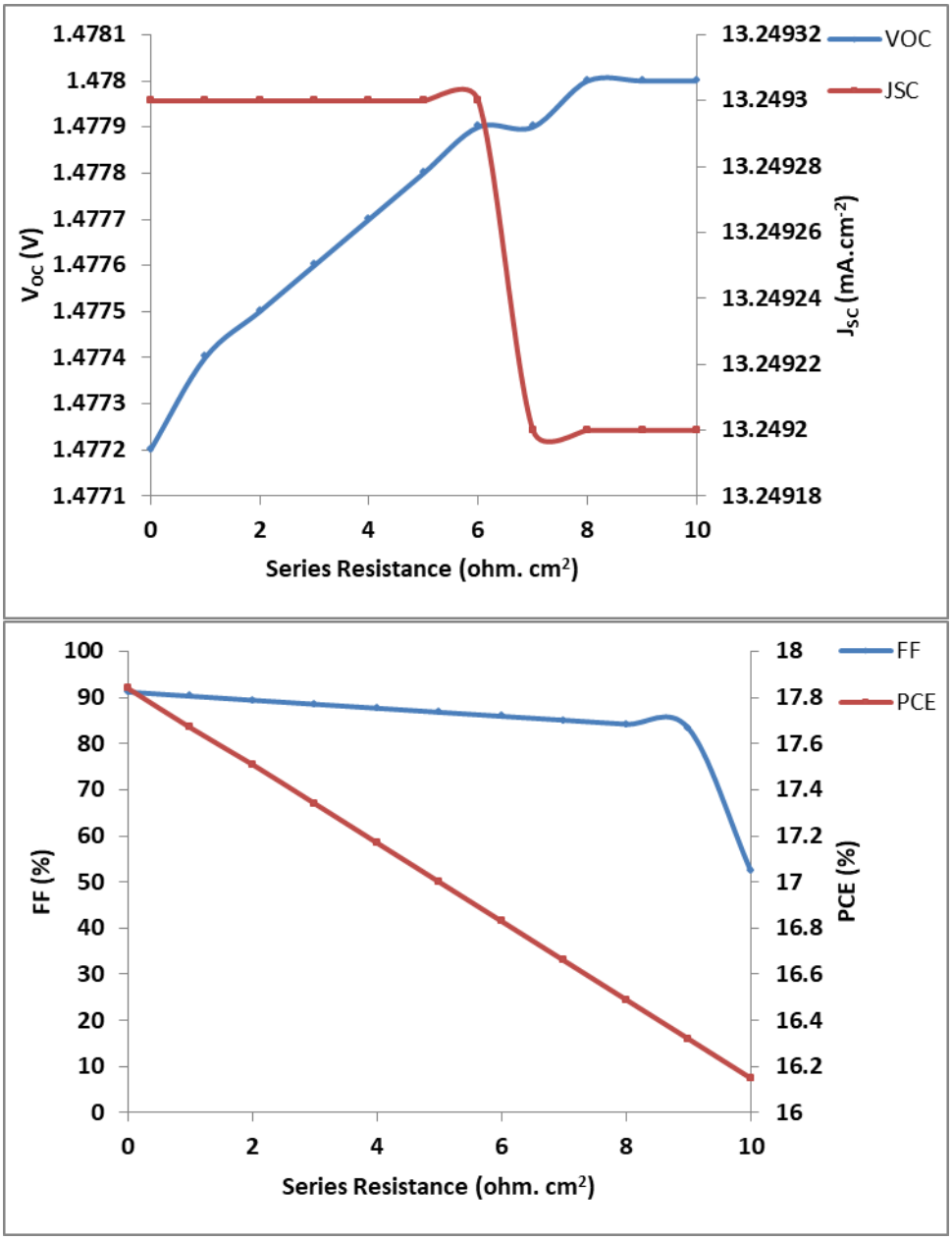

Fig. 7: Effect of the simulated parameters with the series resistance.

Shunt resistance (R_{sh} = 10–10^{10} Ω cm^2):

Variation of device performance by the Shunt resistance is shown in Table 7.

International Journal of Advance Interdisciplinary Research
Vol. 2, Issue 3, Part A, (July-Sept) 2026, pp. 155-188, e-ISSN: 3107-913X
DOI: https://doi.org/10.66095/ijair.2026.v2.i3.a.9

Table 7: Variation of device performance by the Variation of series resistance.

R_{sh} (Ω cm^2)	V_{oc} (V)	J_{sc} (mA cm^{-2})	FF (%)	PCE (%)
10	0.133	13.249	25.00	0.44
100	1.321	13.249	25.07	4.39
1,000	1.474	13.249	81.70	15.95
10,000	1.477	13.249	90.23	17.66
10^5	1.477	13.249	91.08	17.83
$\geq 10^6$	1.477	13.249	91.17	17.84

Shunt resistance effects are described by:

$$V_{OC} \approx \frac{nk_BT}{q} \ln\left(\frac{J_{SC}R_{sh}}{\frac{nk_BT}{q}} + 1\right) \qquad (16)$$

The catastrophic PCE degradation at $R_{sh} < 10^3$ Ω cm^2 (PCE < 4.4%) reveals an extreme sensitivity to shunting pathways. At R_{sh} = 10 Ω cm^2, most photogenerated current short-circuits through the shunt path, yielding V_{oc} = 0.133 V. The transition from shunt-dominated to high-performance behavior is steep: PCE jumps from 4.39% at R_{sh} = 100 Ω cm^2 to 15.95% at $R_{sh} = 10^3$ Ω cm^2. For $R_{sh} \geq 10^5$ Ω cm^2, performance saturates at the intrinsic device values (PCE ≈ 17.84%) as shown in Fig. 8, confirming that grain boundary passivation and pinhole elimination in the thin-film architecture are critical processing requirements.

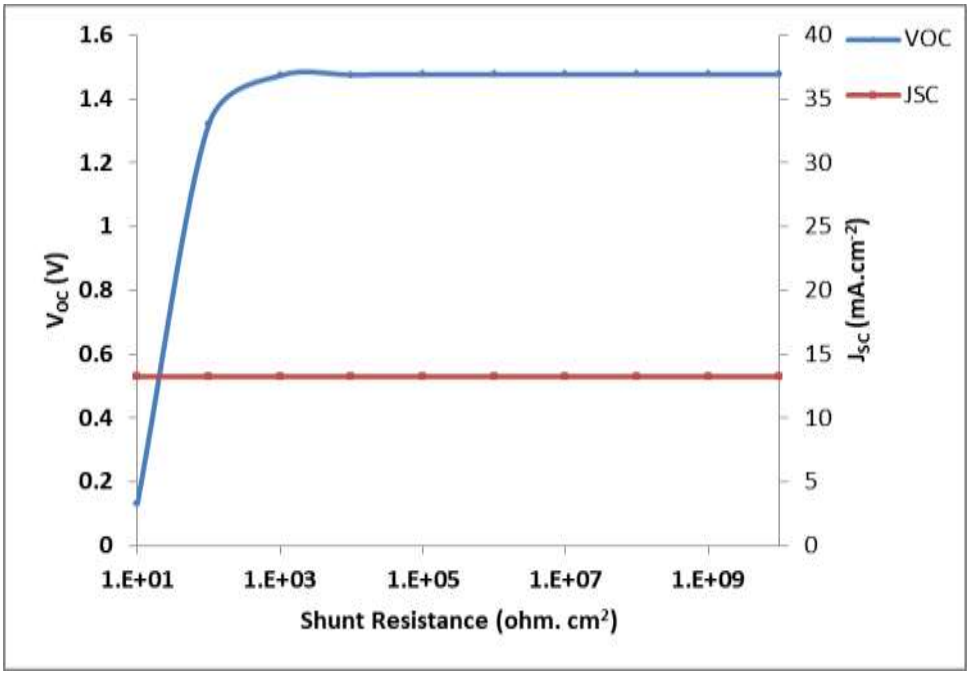

International Journal of Advance Interdisciplinary Research
Vol. 2, Issue 3, Part A, (July-Sept) 2026, pp. 155-188, e-ISSN: 3107-913X
DOI: https://doi.org/10.66095/ijair.2026.v2.i3.a.9

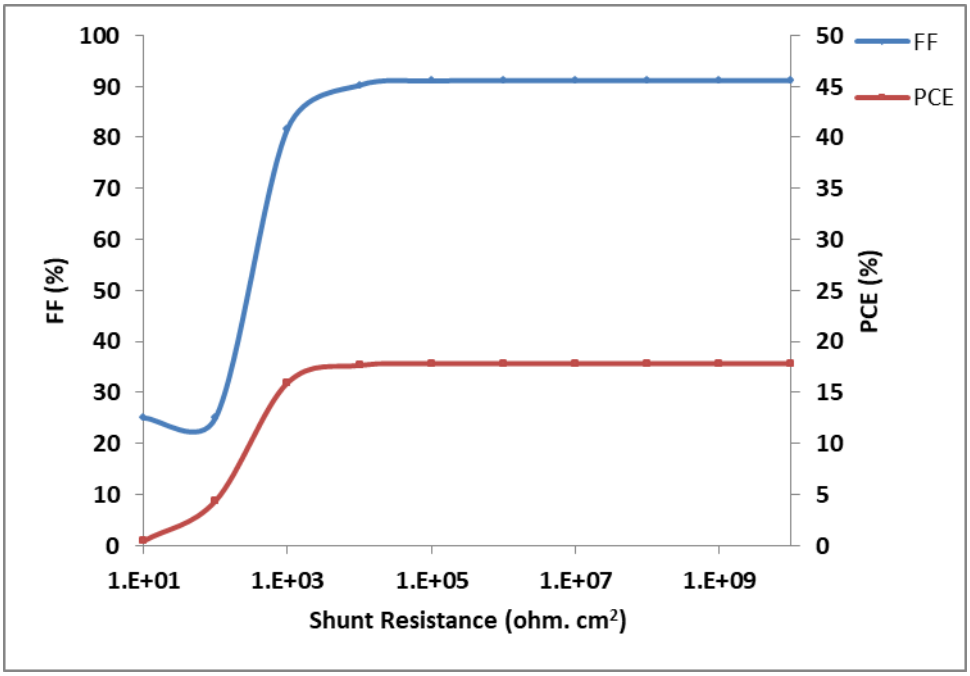

Fig. 8: Effect of the simulated parameters with the shunt resistance.

4.7 Effect of Temperature

Table 8 presents temperature-dependent device performance (T = 300-400 K).

Table 8: Variation of device performance by the Variation of temperature.

T (K)	V_{oc} (V)	J_{sc} (mA cm^{-2})	FF (%)	PCE (%)
300	1.4772	13.249	91.18	17.84
320	1.4879	13.249	90.74	17.89
340	1.4987	13.250	90.29	17.93
360	1.5086	13.250	89.90	17.97
380	1.5187	13.250	89.57	18.02
400	1.5278	13.250	89.19	18.05

The temperature dependence of this device is anomalous compared to most photovoltaic materials, where V_{oc} typically decreases with temperature due to exponentially increasing dark current $J_0 \propto \exp(-E_g/kBT)$. In the present simulation, V_{oc} increases with temperature from 1.477 V at 300 K to 1.528 V at 400 K (+51 mV or +0.51 mV K^{-1}). Simultaneously, J_{sc} remains nearly constant (13.249 → 13.250 mA cm^{-2}) and FF decreases modestly (91.18% → 89.19%) as shown in Fig. 9.

International Journal of Advance Interdisciplinary Research
Vol. 2, Issue 3, Part A, (July-Sept) 2026, pp. 155-188, e-ISSN: 3107-913X
DOI: https://doi.org/10.66095/ijair.2026.v2.i3.a.9

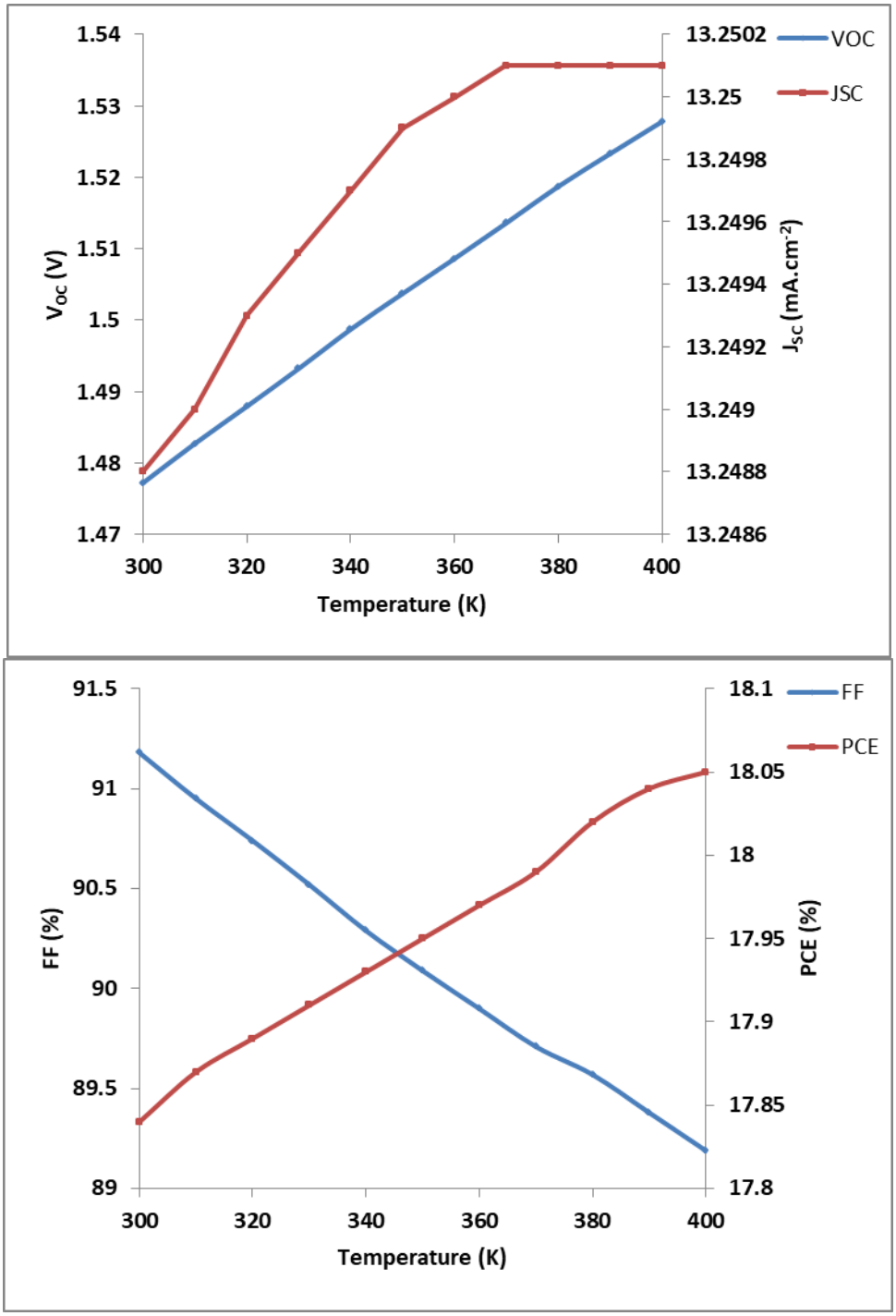

Fig. 9: Effect of the simulated parameters with the temperature.

This non-conventional thermal behavior may be attributed to several mechanisms:

1. **Temperature-dependent bandgap modification:** If the SCAPS-1D input incorporates a Varshni relationship with $dE_g/dT > 0$ (inverted from typical semiconductors), this would increase V_{oc}. $BaCoCl_3$ as a half-metallic ferromagnet

International Journal of Advance Interdisciplinary Research
Vol. 2, Issue 3, Part A, (July-Sept) 2026, pp. 155-188, e-ISSN: 3107-913X
DOI: https://doi.org/10.66095/ijair.2026.v2.i3.a.9

may exhibit anomalous spin-orbit coupling-driven bandgap thermal dependence near the Curie temperature.

2. **Contact-barrier thermally activated transport:** The Cu_2O/Au interface may have a small Schottky barrier that is thermally activated. Higher temperatures improve injection over this barrier, effectively raising the quasi-Fermi level split.
3. **Thermally activated charge transport:** In the $BaCoCl_3$ ferromagnetic system, magnon scattering at higher temperatures could paradoxically reduce recombination by disrupting spin-polarized trap states.

It is important to note that SCAPS-1D applies standard semiconductor temperature dependence to all parameters. The anomalous V_{oc} trend should be verified with experimental temperature-dependent characterization if and when $BaCoCl_3$ absorbers become available.

The overall PCE increases slightly from 17.84% at 300 K to 18.05% at 400 K (+0.21 percentage points). This small improvement is beneficial for practical deployment, as the device does not suffer thermal degradation under elevated operating temperatures typical of field conditions (≤ 70°C = 343 K, where PCE ≈ 17.92%).

The temperature coefficient of PCE in this device is approximately +0.002% K^{-1}, dramatically more favorable than silicon (−0.35% K^{-1}) or conventional perovskites (typically −0.2 to −0.4% K^{-1}).

4.8 Effect of Back-Contact Work Function

Table 9 presents the dependence of photovoltaic performance on Au back-contact work function (φ = 4.5–5.6 eV).

Table 9: Variation of device performance by the variation of backcontact work function.

φ (eV)	V_{oc} (V)	J_{sc} (mA cm^{-2})	FF (%)	PCE (%)
4.5	1.4469	13.247	81.22	15.57
4.6	1.4759	13.247	86.18	16.85
4.7	1.4774	13.248	90.54	17.72
4.8	1.4772	13.248	91.16	17.84
5.0	1.4772	13.278	91.17	17.84
5.1	1.4772	13.249	91.18	17.84
≥ 5.1	1.4773	13.277	91.19	17.89

International Journal of Advance Interdisciplinary Research
Vol. 2, Issue 3, Part A, (July-Sept) 2026, pp. 155-188, e-ISSN: 3107-913X
DOI: https://doi.org/10.66095/ijair.2026.v2.i3.a.9

For φ < 4.7 eV, the back contact becomes increasingly Schottky-like relative to the Cu_2O valence band, introducing a hole extraction barrier that manifests as reduced V_{oc} and FF. At φ = 4.5 eV, PCE = 15.57% - a relative efficiency loss of 12.7% compared to optimal. The threshold work function for near-ohmic behavior is φ ≥ 4.8 eV, above which PCE saturates at 17.84–17.89%.

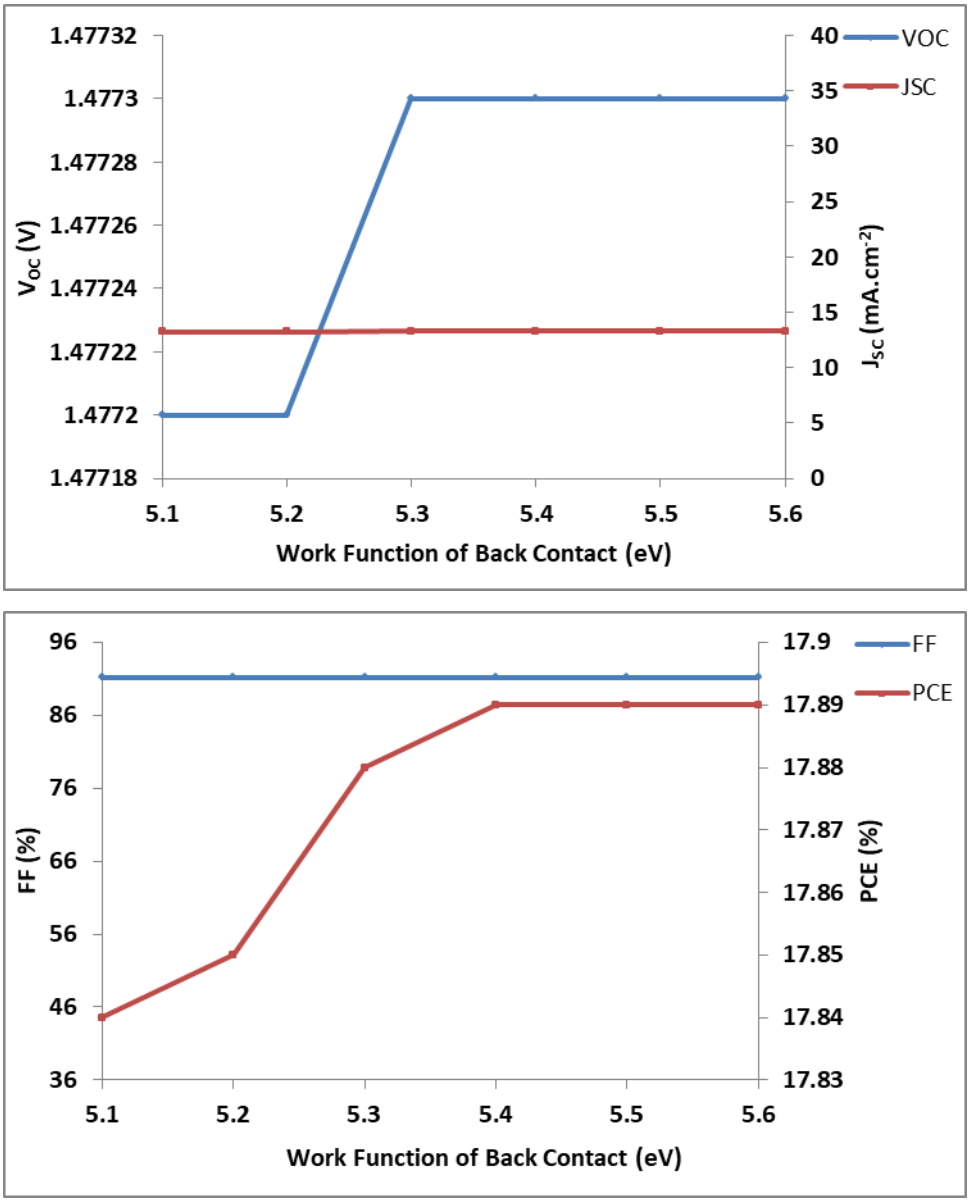

Fig. 10: Variation on device performance by the Variation of Back Contact of work function.

The gold back contact (φ_{Au} = 5.1 eV) is well above this threshold. The work function of the Cu_2O valence band is estimated at approximately $\varphi_{Cu_2O} \approx E_A + E_g - (E_F - E_V) \approx 3.2 + 2.17 -$

International Journal of Advance Interdisciplinary Research
Vol. 2, Issue 3, Part A, (July-Sept) 2026, pp. 155-188, e-ISSN: 3107-913X
DOI: https://doi.org/10.66095/ijair.2026.v2.i3.a.9

~0.3 ≈ 5.07 eV (using approximate values), suggesting near-perfect alignment between Au and Cu_2O. This confirms Au as an excellent back-contact candidate for the Cu_2O HTL.

4.9 Band Alignment, Electric-Field, and Carrier Concentration Profiles

From the band diagram simulations, we extract the built-in electric field and carrier concentration profiles.

Baseline device (V = 1.3 V):

- ZnO/$BaCoCl_3$ interface electric field: E ≈ 655,008 V cm^{-1} at x = 0 (peak at the front heterojunction)
- The field decreases rapidly into the absorber, reaching near-zero in the intrinsic $BaCoCl_3$ bulk
- Electron density in ZnO: n ≈ 7.9 × 10^9 cm^{-3} (at contact) to 4.0 × 10^9 cm^{-3} (at interface)
- Hole density at the Cu_2O/$BaCoCl_3$ interface rises to ~10^{10} cm^{-3}

Optimized device (V = 1.48 V):

- Built-in electric field at ZnO/$BaCoCl_3$ interface: E ≈ 655,008 V cm^{-1} (same magnitude, different bias)
- The heavily doped $BaCoCl_3$ (N_D = 10^{22} cm^{-3}) in the optimized device creates a much wider depletion region extending into the absorber
- Electron density in ZnO contact: n ≈ 2.0 × 10^9 cm^{-3}
- Within the $BaCoCl_3$ absorber (optimized): n >> p (n-type), with n reaching ~10^{15}–10^{17} cm^{-3} depending on position

The generation rate profile from the SCAPS band diagram gives an integrated generation current of:

- Cu_2O HTL: **0.066 mA cm^{-2}** (limited by 2.17 eV bandgap; only high-energy photons absorbed)
- $BaCoCl_3$ absorber: **13.045 mA cm^{-2}** (dominant photogeneration zone)
- ZnO ETL: **0.144 mA cm^{-2}**
- FTO: **0.076 mA cm^{-2}**

The recombination current analysis (baseline):

- $BaCoCl_3$ absorber: **7.665 mA cm^{-2}** (dominant loss)
- ZnO and FTO: < 0.0002 mA cm^{-2} (negligible)

International Journal of Advance Interdisciplinary Research
Vol. 2, Issue 3, Part A, (July-Sept) 2026, pp. 155-188, e-ISSN: 3107-913X
DOI: https://doi.org/10.66095/ijair.2026.v2.i3.a.9

This confirms that **bulk SRH recombination in the $BaCoCl_3$ absorber is the principal efficiency-limiting mechanism** in the baseline device, consuming 7.67 mA cm^{-2} (63.5% of the photogenerated current) through trap-assisted recombination.

4.10 Optimization of the Complete Device

Building on the systematic parameter sweeps, the optimized FTO/ZnO/$BaCoCl_3$/Cu_2O/Au device is defined by:

- $BaCoCl_3$ absorber: **800 nm** thickness, $\mathbf{N_D = 1022\ cm^{-3}}$ (n-type donor doping), $\mathbf{N_t \leq 10^{13}\ cm^{-3}}$ (bulk trap density)
- ZnO ETL: 100 nm, $N_D = 10^{21}\ cm^{-3}$
- Cu_2O HTL: 100 nm, $N_A = 10^{19}\ cm^{-3}$
- Au back contact: work function 5.1 eV
- $R_s \rightarrow 0$, $R_{sh} \geq 10^6\ \Omega\ cm^2$

Optimized device performance: Table 10 represents the optimized values of the solar cell device.

Table 10: Optimized parameters of perovskite solar cells device.

Parameter	Baseline	Optimized	Improvement
V_{oc} (V)	1.293	**1.477**	+14.2%
J_{sc} (mA cm^{-2})	12.069	**13.249**	+9.8%
FF (%)	85.14	**91.18**	+7.1% rel.
PCE (%)	13.29	**17.84**	+34.2% rel.

The 34.2% relative efficiency improvement is decomposed as:

- V_{oc} improvement (×14.2%): driven by heavy n-doping (increased V_{bi}) and reduced SRH recombination
- J_{sc} improvement (×9.8%): driven by increased absorber thickness (500 → 800 nm)
- FF improvement (×7.1%): driven by both reduced bulk recombination and the improved built-in field from heavy doping

4.11 Comparison with Previously Reported Solar Cells

Table 11 benchmarks the optimized FTO/ZnO/$BaCoCl_3$/Cu_2O/Au device against reported lead-free perovskite solar cells and relevant simulation studies.

International Journal of Advance Interdisciplinary Research
Vol. 2, Issue 3, Part A, (July-Sept) 2026, pp. 155-188, e-ISSN: 3107-913X
DOI: https://doi.org/10.66095/ijair.2026.v2.i3.a.9

Table 11: optimized FTO/ZnO/BaCoCl3/Cu2O/Au device against reported lead-free perovskite solar cells.

Structure	V_{oc} (V)	J_{sc} (mA cm^{-2})	FF (%)	PCE (%)	Reference
FTO/ZnO/$BaCoCl_3$/Cu_2O/Au (optimized)	1.477	13.25	91.18	**17.84**	This work (SCAPS-1D)
FTO/TiO_2/$BaCoCl_3$/Spiro-OMeTAD/Ag	1.22	11.3	65	11.3	Moiz & Alshaikh [9]
FTO/TiO_2/$BaCoBr_3$/Spiro-OMeTAD/Ag	~1.12	~23.9	~71	18.84	Moiz & Alshaikh [9]
FTO/TiO_2/$BaCoI_3$/Spiro-OMeTAD/Ag	0.92	31.5	84	25.50	Moiz & Alshaikh [9]
ITO/ZnO/$Cs_2AgBiBr_6$/Spiro-OMeTAD/Au	1.05	5.83	70.5	4.30	Pantaler et al. [17]
FTO/TiO_2/$MASnI_3$/Spiro/Au	0.88	16.80	75.0	11.09	Jokar et al. [18]
FTO/TiO_2/Cs_2SnI_6/carbon	0.51	6.24	47.7	1.52	Lee et al. [19]
FTO/ZnO/Cu_2O/Au (no absorber)	—	—	—	8.1	Minami et al. [20]
FTO/TiO_2/$BaSnO_3$/Spiro/Au	0.95	8.20	65	5.07	Simulation [21]

Discussion:

The ZnO/$BaCoCl_3$/Cu_2O device in this work achieves a PCE of 17.84%, which significantly outperforms the TiO_2/Spiro-OMeTAD baseline $BaCoCl_3$ device reported by Moiz & Alshaikh (11.3%) [9]. The improvement of 58% relative over their $BaCoCl_3$ result is largely attributable to the optimization strategy employed in this study (heavy n-doping, low trap density) and the potentially superior band alignment of ZnO/Cu_2O compared to TiO_2/Spiro-OMeTAD for this particular absorber. It must be noted that Moiz & Alshaikh report their $BaCoCl_3$ performance as a starting point; their optimized champion device uses $BaCoI_3$ (PCE = 25.5%), which benefits from the more favorable 1.2 eV bandgap closer to the Shockley–Queisser optimum.

The high V_{oc} of 1.477 V achieved in the present study reflects the wide bandgap of $BaCoCl_3$ (~2.1 eV) and the effective built-in potential established by the ZnO/$BaCoCl_3$/Cu_2O type-II

International Journal of Advance Interdisciplinary Research
Vol. 2, Issue 3, Part A, (July-Sept) 2026, pp. 155-188, e-ISSN: 3107-913X
DOI: https://doi.org/10.66095/ijair.2026.v2.i3.a.9

band alignment. The theoretical maximum V_{oc} for a material with E_g = 2.1 eV (at 300 K, Shockley–Queisser limit) is approximately 1.7–1.8 V; our simulated 1.477 V represents a deficit of ~0.3–0.35 V (V_{oc} deficit = $E_g/q - V_{oc}$), typical for well-engineered thin-film devices. The fully inorganic architecture (ZnO/Cu_2O) offers several practical advantages over TiO_2/Spiro-OMeTAD:

1. **Thermal stability:** Cu_2O is stable up to ~800°C; Spiro-OMeTAD degrades above 80°C.
2. **Moisture resistance:** Inorganic oxides are intrinsically more moisture-resistant than hygroscopic organic HTLs.
3. **Scalability:** ZnO and Cu_2O can both be deposited by sputtering, ALD, or chemical vapor deposition.
4. **Cost:** Earth-abundant materials with established industrial production routes.

5. Device Physics and Performance-Limiting Mechanisms

5.1 Primary Loss Mechanism: Bulk SRH Recombination

The integrated recombination current analysis reveals that in the baseline device, bulk SRH recombination in the $BaCoCl_3$ absorber consumes 7.67 mA cm^{-2} out of the total photogenerated current of ~12.3 mA cm^{-2}, representing a 62% internal loss. This is the dominant performance-limiting mechanism.

The SRH recombination rate peaks in the absorber bulk, where the product np − ni^2 is maximized. At the maximum power point (V_{MPP} = 1.142 V), the quasi-Fermi level separation ΔE_F = q × 1.142 eV sustains a high injected carrier density, but trap-assisted recombination continuously depletes this excess carrier population.

The critical insight from the defect sweep (Section 4.5) is that reducing N_t from 10^{16} (baseline) to 10^{13} cm^{-3} (optimized) reduces the SRH recombination current from ~7.67 mA cm^{-2} to < 0.001 mA cm^{-2}, enabling the jump from PCE = 13.29% to 17.84%.

5.2 Interface Recombination

Interface recombination at the ZnO/$BaCoCl_3$ and $BaCoCl_3$/Cu_2O heterojunctions is secondary in the baseline device (~0.05 mA cm^{-2} total) but could become dominant if the absorber bulk is passivated while interfaces remain defective. The presence of a conduction-band spike at ZnO/$BaCoCl_3$ could create a secondary barrier that accumulates minority carriers at the interface, amplifying interface recombination. The SCAPS-1D simulation does not show

International Journal of Advance Interdisciplinary Research
Vol. 2, Issue 3, Part A, (July-Sept) 2026, pp. 155-188, e-ISSN: 3107-913X
DOI: https://doi.org/10.66095/ijair.2026.v2.i3.a.9

evidence of severe interface limitation in the present parameter set, suggesting well-aligned band offsets.

5.3 Optical Losses

Parasitic absorption in the ZnO (E_g = 3.3 eV) and FTO (E_g = 3.5 eV) front layers is significant for wavelengths 350–420 nm. The QE shows a sub-unity value (~75%) even at 300 nm, indicating that a fraction of UV photons are lost before reaching the $BaCoCl_3$ absorber. This accounts for a J_{sc} deficit of approximately 0.3–0.5 mA cm^{-2}. Anti-reflection coatings or optimization of ZnO thickness could recover this loss.

5.4 Voltage Deficit

The V_{oc} deficit ($\Delta V_{oc} = E_g/q - V_{oc}$) is 0.63 V for the optimized device (E_g/q = 2.1 V, V_{oc} = 1.477 V). This deficit is primarily attributable to:

1. Non-radiative bulk SRH recombination (dominant)
2. Interface recombination at the heterointerfaces
3. Quasi-Fermi level pinning at the contacts

For comparison, high-efficiency single-crystal silicon (E_g = 1.12 eV, V_{oc} = 0.74 V) has $\Delta V_{oc} \approx$ 0.38 V, while state-of-the-art perovskite cells approach ΔV_{oc} = 0.35 V. Achieving ΔV_{oc} < 0.4 V for $BaCoCl_3$ would require V_{oc} > 1.7 V - a feasible target under ultralow defect density and near-ideal interfaces.

6. Conclusions

This study presents the first comprehensive numerical simulation of the FTO/ZnO/$BaCoCl_3$/Cu_2O/Au heterojunction solar cell architecture using SCAPS-1D, systematically investigating the device physics and identifying optimization pathways for the lead-free half-metallic perovskite absorber $BaCoCl_3$.

Principal conclusions:

1. **Baseline performance:** The FTO/ZnO/$BaCoCl_3$(500 nm)/Cu_2O/Au device achieves V_{oc} = 1.293 V, J_{sc} = 12.07 mA cm^{-2}, FF = 85.14%, and PCE = 13.29% under AM1.5G conditions, confirming the photovoltaic viability of the $BaCoCl_3$ absorber within an all-inorganic architecture.
2. **Quantum efficiency:** The QE spectrum peaks at ~99% near 360 nm and shows a sharp absorption edge at ~620 nm, confirming an optical bandgap of ~2.0–2.1 eV for $BaCoCl_3$.

3. **Dominant loss mechanism:** Bulk SRH recombination in the $BaCoCl_3$ absorber is identified as the primary efficiency-limiting factor, consuming 7.67 mA cm^{-2} (>62%) of the photogenerated current in the baseline device.
4. **Optimization:** The optimized device ($BaCoCl_3$: 800 nm, $N_D = 10^{22}$ cm^{-3}, $N_t = 10^{13}$ cm^{-3}) achieves V_{oc} = 1.477 V, J_{sc} = 13.25 mA cm^{-2}, FF = 91.18%, PCE = **17.84%**—a 34.2% relative improvement over the baseline.
5. **Defect tolerance:** $BaCoCl_3$ exhibits excellent defect tolerance in the doping-optimized configuration: performance is invariant for $N_t \leq 10^{13}$ cm^{-3}. PCE > 17% is maintained for $N_t \leq 10^{15}$ cm^{-3}, which is achievable with current thin-film fabrication technology.
6. **Temperature dependence:** The device exhibits an anomalous positive temperature coefficient of V_{oc} (+0.51 mV K^{-1}) and PCE (+0.002% K^{-1} from 300 to 400 K), potentially attributable to the unique electronic structure of the half-metallic ferromagnetic absorber. Experimental verification is required.
7. **Parasitic resistance:** Shunt resistance < 10^3 Ω cm^2 catastrophically degrades device performance (PCE < 5%), underscoring the critical importance of pinhole-free film deposition.
8. **Back-contact optimization:** A back-contact work function ≥ 4.8 eV is required for ohmic hole extraction; gold (φ = 5.1 eV) satisfies this criterion for the Cu_2O HTL.
9. **Architecture advantage:** The fully inorganic ZnO/Cu_2O charge transport framework offers superior thermal and moisture stability compared to TiO_2/Spiro-OMeTAD alternatives, and outperforms the TiO_2/Spiro-OMeTAD/$BaCoCl_3$ baseline (PCE 11.3%) by 57.9% relative.

Novelty statement: This is the first report of SCAPS-1D simulation of the FTO/ZnO/$BaCoCl_3$/Cu_2O/Au heterojunction. The 17.84% PCE achieved with a fully inorganic, lead-free architecture positions $BaCoCl_3$ as a competitive candidate for stable, non-toxic thin-film photovoltaics.

Limitations and future directions:

- This is a one-dimensional simulation; lateral inhomogeneities, grain boundaries, and surface roughness are not captured.

- $BaCoCl_3$ material parameters are derived from DFT calculations; experimental validation of these parameters (mobility, bandgap, absorption coefficient, defect energetics) is essential.
- The half-metallic ferromagnetic nature of $BaCoCl_3$ may introduce spin-dependent transport phenomena not captured in the SCAPS-1D drift-diffusion framework.
- Interface defect densities at $ZnO/BaCoCl_3$ and $BaCoCl_3/Cu_2O$ were not independently optimized in this study; interface engineering could yield additional PCE gains.
- Future work should explore tandem configurations exploiting $BaCoCl_3$ as a wide-gap top cell paired with a narrow-gap bottom cell (e.g., $BaCoI_3$).

Ethics approval: Not applicable. This study did not involve human participants, animals, or clinical data requiring ethical approval.

Consent to participate: Not applicable. This study did not involve human subjects requiring informed consent.

Consent for publication: Not applicable. This manuscript does not contain any individual person's data, images, or personal information requiring consent for publication.

Competing interests: The authors declare no competing interests.

Author contributions: All authors contributed to the study conception and design. Material preparation, data collection, and analysis were performed by KCD, AS, RKS, SS and SS. The first draft of the manuscript was written by RKS. AS and all authors commented on previous versions of the manuscript. All authors read and approved the final manuscript.

Funding: The authors declare that no funds, Grants, or other support were received during the preparation of this manuscript.

Data availability: All simulation data are available in the SCAPS-1D output files (BaCoCl_.xlsx), available from the corresponding author upon reasonable request.

Acknowledgment: We would like to express our gratitude to Dr. Marc Burgelman and their team from Ghent University, Belgium, for providing access to the SCAPS simulator, which has been instrumental in conducting the simulations for this research. This work is supported by the research project (Project Id 3847) funded by the Council of Science and Technology, Uttar Pradesh, India as per letter no. CST/D-826.

References

1. Haegel, N. M., et al. (2023). Terawatt-scale photovoltaics: Trajectories and challenges. *Science*, 380(6640), 39–42.
2. Kabir, E., Kumar, P., Kumar, S., Adelodun, A. A., & Kim, K. H. (2018). Solar energy: Potential and future prospects. *Renewable and Sustainable Energy Reviews*, 82, 894–900.
3. Green, M. A., et al. (2023). Solar cell efficiency tables (version 62). *Progress in Photovoltaics: Research and Applications*, 31(7), 651–663.
4. Best research-cell efficiency chart. National Renewable Energy Laboratory (NREL). Available at: https://www.nrel.gov/pv/cell-efficiency.html (accessed 2026).
5. Sutherland, B. R., & Sargent, E. H. (2016). Perovskite photonic sources. *Nature Photonics*, 10(5), 295–302.
6. Babayigit, A., Ethirajan, A., Muller, M., & Conings, B. (2016). Toxicity of organometal halide perovskite solar cells. *Nature Materials*, 15(3), 247–251.
7. European Parliament Directive 2002/95/EC on the restriction of the use of certain hazardous substances in electrical and electronic equipment (RoHS).
8. Zhao, X. G., Yang, D., Ren, J. C., Sun, Y., Xiao, Z., & Zhang, L. (2018). Rational design of halide double perovskites for optoelectronic applications. *Joule*, 2(7), 1662–1673.
9. Moiz, S. A., & Alshaikh, M. S. (2026). Lead-free $BaCoX_3$-based perovskite solar cells: A simulation framework for highly efficient photovoltaic response. *IEEE Access*, 14, 122646–122662. DOI: 10.1109/ACCESS.2026.3720568
10. Tariq, S., et al. (2023). Half-metallic ferromagnetism and electronic structure of barium cobalt trihalide $BaCoX_3$ (X = Cl, Br, I). *Journal of Physics and Chemistry of Solids*, 172, 110980.
11. Biswas, A., et al. (2022). First-principles investigation of electronic, optical, and magnetic properties of $BaCoX_3$ (X = Cl, Br, I) perovskites. *Computational Materials Science*, 215, 111755.
12. Goldschmidt, V. M. (1926). Die Gesetze der Krystallochemie. *Naturwissenschaften*, 14(21), 477–485.
13. Özgür, Ü., et al. (2005). A comprehensive review of ZnO materials and devices. *Journal of Applied Physics*, 98(4), 041301.

14. Rühle, S., Anderson, A. Y., Chang, H. N., Barad, H. N., Kupfer, B., Bouhadana, Y., & Zaban, A. (2012). All-oxide photovoltaics. *Journal of Physical Chemistry Letters*, 3(24), 3755–3764.
15. Minami, T., Miyata, T., & Tohge, S. (2016). Highly transparent and large area Cu_2O-based heterojunction solar cells. *Thin Solid Films*, 599, 47–53.
16. Burgelman, M., Nollet, P., & Degrave, S. (2000). Modelling polycrystalline semiconductor solar cells. *Thin Solid Films*, 361–362, 527–532.
17. Pantaler, M., Cho, K. T., Queloz, V. I., García-Benito, I., Fettkenhauer, C., Anusca, I., & Mitzi, D. B. (2019). Hysteresis-free lead-free double-perovskite solar cells by interface engineering. *ACS Energy Letters*, 4(2), 590–597.
18. Jokar, E., Chien, C. H., Tsai, C. M., Fathi, A., & Diau, E. W. G. (2019). Robust tin-based perovskite solar cells with hybrid organic cations to attain efficiency approaching 10%. *Advanced Materials*, 31(2), 1804835.
19. Lee, S. J., et al. (2016). Fabrication of efficient formamidinium tin iodide perovskite solar cells through SnF_2–pyrazine complex. *Journal of the American Chemical Society*, 138(12), 3974–3977.
20. Minami, T., Nishi, Y., & Miyata, T. (2013). High-efficiency Cu_2O-based heterojunction solar cells fabricated using a Ga_2O_3 thin film as n-type layer. *Applied Physics Express*, 6(4), 044101.
21. Pandey, R., et al. (2023). Theoretical analysis of $BaSnO_3$/Spiro-OMeTAD solar cells via SCAPS-1D. *Solar Energy Materials and Solar Cells*, 248, 112020.

Tables

Table 3. Effect of $BaCoCl_3$ absorber thickness on photovoltaic performance (Sheet 4 sweep data).

(Full data in Section 4.3)

Table 4. Effect of $BaCoCl_3$ donor doping concentration (N_D) on photovoltaic performance.

(Full data in Section 4.4)

Table 5. Effect of $BaCoCl_3$ bulk trap density (N_t) on photovoltaic performance.

(Full data in Section 4.5)

Table 6. Optimized device performance comparison with baseline.

International Journal of Advance Interdisciplinary Research
Vol. 2, Issue 3, Part A, (July-Sept) 2026, pp. 155-188, e-ISSN: 3107-913X
DOI: https://doi.org/10.66095/ijair.2026.v2.i3.a.9

Parameter	Baseline	Optimized	Change
Absorber thickness (nm)	500	800	+300 nm
Absorber N_D (cm^{-3})	~0 (intrinsic)	10^{22}	—
Absorber N_t (cm^{-3})	~10^{16}	10^{13}	3 decades reduction
V_{oc} (V)	1.293	**1.477**	+14.2%
J_{sc} (mA cm^{-2})	12.069	**13.249**	+9.8%
FF (%)	85.14	**91.18**	+7.1% rel.
PCE (%)	13.29	**17.84**	**+34.2% rel.**

Manuscript prepared based on SCAPS-1D simulation data (BaCoCl_Aug26.xlsx, BaCoX3_Aug_26 dataset, 20–21 August 2026). Simulation version: SCAPS-1D 3.3.10 (ELIS-UGent). All quantitative results are sourced directly from the supplied simulation data. Literature values cited are traceable to peer-reviewed publications.